Spinel LiMn$_2$O$_4$ integrated with coating and doping by Sn self-segregation

Huaifang Shang and Dingguo Xia

Articles you may be interested in

Yong Zhang, Zhao-hui Guo, Zi-yu Han, Xi-yuan Xiao, and Chi Peng, Feasibility of aluminum recovery and MgAl$_2$O$_4$ spinel synthesis from secondary aluminum dross, *Int. J. Miner. Metall. Mater.*, 26(2019), No. 3, pp. 309-318. https://doi.org/10.1007/s12613-019-1739-3

Qi-qiang Mou, Jian-li Li, Qiang Zeng, and Hang-yu Zhu, Effect of Fe$_2$O$_3$ on the size and components of spinel crystals in the CaO-SiO$_2$-MgO-Al$_2$O$_3$-Cr$_2$O$_3$ system, *Int. J. Miner. Metall. Mater.*, 26(2019), No. 9, pp. 1113-1119. https://doi.org/10.1007/s12613-019-1822-9

Rowaid Al-khazraji, Ya-qiong Li, and Li-feng Zhang, Boron separation from Si-Sn alloy by slag treatment, *Int. J. Miner. Metall. Mater.*, 25(2018), No. 12, pp. 1439-1446. https://doi.org/10.1007/s12613-018-1698-0

Seyed Esmaiel Shakib, Ramin Raiszadeh, and Jalil Vahdati-Khaki, A Self-propagating high-temperature synthesis process for the fabrication of Fe(Cr)-Al$_2$O$_3$ nanocomposite, *Int. J. Miner. Metall. Mater.*, 26(2019), No. 6, pp. 775-786. https://doi.org/10.1007/s12613-019-1779-8

Peng Jiang, Guo-xiang Yin, Ming-wei Yan, Jia-lin Sun, Bin Li, and Yong Li, A new synthetic route to MgO-MgAl$_2$O$_4$-ZrO$_2$ highly dispersed composite material through formation of Mg$_5$Al$_{2.4}$Zr$_{1.7}$O$_{12}$ metastable phase:synthesis and physical properties, *Int. J. Miner. Metall. Mater.*, 24(2017), No. 3, pp. 332-341. https://doi.org/10.1007/s12613-017-1412-7

K. Sanesh, S. Shiam Sunder, and N. Radhika, Effect of reinforcement content on the adhesive wear behavior of Cu10Sn5Ni/Si$_3$N$_4$ composites produced by stir casting, *Int. J. Miner. Metall. Mater.*, 24(2017), No. 9, pp. 1052-1060. https://doi.org/10.1007/s12613-017-1495-1

IJMMM WeChat   QQ author group

Spinel LiMn₂O₄ integrated with coating and doping by Sn self-segregation

Huaifang Shang[1] *and Dingguo Xia*[2],✉

1) Key Laboratory of Magnetic Molecules and Magnetic Information Materials (Ministry of Education), School of Chemistry and Material Science, Shanxi Normal University, Taiyuan 030031, China

2) Beijing Key Laboratory of Theory and Technology for Advanced Batteries Materials, School of Materials Science and Engineering, Peking University, Beijing 100871, China

Abstract: The development of high-performance and low-cost cathode materials is of great significance for the progress in lithium-ion batteries. The use of Co and even Ni is not conducive to the sustainable and healthy development of the power battery industry owing to their high cost and limited resources. Here, we report $LiMn_2O_4$ integrated with coating and doping by Sn self-segregation. Auger electron energy spectrum and soft X-ray absorption spectrum show that the coating is Sn-rich $LiMn_2O_4$, with a small Sn doping in the bulk phase. The integration strategy can not only mitigate the Jahn−Teller distortion but also effectively avoid the dissolution of manganese. The as-obtained product demonstrates superior high initial capacities of 124 mAh·g⁻¹ and 120 mAh·g⁻¹ with the capacity retention of 91.1% and 90.2% at 25°C and 55°C after 50 cycles, respectively. This novel material-processing method highlights a new development direction for the progress of cathode materials for lithium-ion batteries.

Keywords: spinel lithium manganate; coating and doping; tin self-segregation; high capacity; good stability

1. Introduction

In recent years, lithium-ion secondary batteries have played a crucial role in the development of modern society as an important energy storage device in portable electronic products and new energy vehicles [1–4]. Layered cathode materials containing cobalt or nickel are among the most promising cathodes for high-energy lithium-ion batteries because of their high capacity and working potential [5–6]. However, due to the high cost and limited resources of cobalt and nickel, it is necessary to develop cobalt-free and nickel-free cathode materials [7–9]. Lithium manganate ($LiMn_2O_4$) spinel is a mainstream commercial cathode material for rechargeable energy storage owing to its stable structure, good safety, high operation voltage, and low cost [10–11]. Batteries with $LiMn_2O_4$ as the cathode are widely used in low-speed electric vehicles and portable electronic products for energy storage [12–13]. However, in its electric vehicle application, the cycle stability of the battery with $LiMn_2O_4$ as the cathode is unable to meet the actual demand when operating at high temperatures for a long time. Thus, the application of $LiMn_2O_4$ in electric vehicle power batteries has been limited. The capacity decay of $LiMn_2O_4$ is closely related to manganese dissolution caused by the Jahn–Teller effect and electrolyte decomposition. To address these problems, several techniques have been employed, such as ion doping, surface coating, and adding electrolyte additive [14–15]. Current research work focuses on inhibiting the Jahn–Teller phase transition from cubic to tetragonal [16–17] and preventing manganese dissolution in the electrolyte [18], especially at a high temperature at which the average valence state of Mn is below 3.5 [19–20]. However, in many cases, either the improvement effect is not satisfactory, or the preparation process is too complex.

Considering the convenience of the preparation and avoiding the surface two-phase lattice mismatch caused by improper coating on the $LiMn_2O_4$ surface, we report for the first time, $LiMn_2O_4$ with Sn-rich coating through Sn surface self-segregation, thus integrating coating and doping. The as-obtained sample delivers superior high initial capacities of 124 mAh·g⁻¹ and 120 mAh·g⁻¹ with the capacity retention of 91.1% and 90.2% at 25°C and 55°C after 50 cycles, respectively. Auger electron spectroscopy (AES), powder X-ray photoelectron spectroscopy (XPS), and near-edge X-ray-absorption fine structure were employed to further reveal the origin of the Sn surface enrichment and the suppression of Jahn–Teller distortion. Sn enrichment on the $LiMn_2O_4$ surface stabilizes the $LiMn_2O_4$ crystal structure and protects the $LiMn_2O_4$ cathode from corrosion induced by organic electrolytes.

2. Experimental

2.1. Synthesis of LMO–Snₓ

First, $LiNO_3$, $Mn(NO_3)_2$, and $SnCl_2$ were weighed at a molar ratio of Li/Mn/Sn = 1.03:(2−x):x with x = 0, 0.005,

✉ Corresponding author: Dingguo Xia   Email: dgxia@pku.edu.cn

Springer

0.01, 0.02, and 0.05, respectively, and completely dissolved into a common solution of purified water with citric acid as a chelating agent. Then, the dried gel was obtained by rotary evaporation at 80°C. Finally, the dried powder was mixed and heated at 850°C for 24 h in the air to obtain the desired materials.

2.2. Characterization

The X-ray diffraction (XRD) measurements were performed using the Bruker D8-ADVANCE diffractometer (Bruker, Germany) with a Cu K_α radiation source (λ = 0.15406 nm). A scanning electron microscope (SEM; Hitachi, S-4800) and a transmission electron microscope (TEM; TECNAI, F20) were used to observe the surface morphology of materials and identify elemental distribution. Transmission electron microscopy (TEM) and high-resolution transmission electron microscopy (HRTEM) were employed to study the microstructure of materials on an F20 transmission electron microscope. Powder XPS (AXIS, ULTRA) was performed to analyze the chemical valence states of elemental Sn and Mn, and the data were calibrated using an indefinite C 1s peak with a fixed value of 284.8 eV. AES (PHI, 700) with 5-keV initial electron energy, 15-nA initial current density, and 9-nm/min sputtering speed was used to determine the element type and material content according to the energy and number of auger electrons emitted by the electron beam laser. The O K-edge X-ray absorption near edge structure (XANES) was measured at beamline 4B7B of the Beijing Synchrotron Radiation Facility. The theoretical simulations of O K-edge X-ray absorption spectroscopy (XAS) were performed within the framework of the multiple-scattering theory [21–22] using the FEFF 8.2 code [23] within the muffin-tin approximation. The FEFF input files were generated using the ATOM package, and the Hedin–Lundqvist exchange correlation potential was selected for the calculations [24]. The occupation of multiple positions by O atoms led to some difficulty in calculating FEFF. XANES technology is a well-known response to the average structural information of the different positions of atomic species. Therefore, during the processing, we first performed the XANES spectroscopy for individual sites, followed by the weighted superposition for all the sites.

2.3. Electrochemical measurements

Electrochemical measurements were performed with the 2032-type coin cells at 25°C and 55°C, respectively, using a Neware battery tester (5 V, 10 mA). Lithium metal was used as the counter electrode. The cathode was prepared by casting a slurry of 80wt% active oxide, 10wt% poly(vinylidene difluoride) binder in N-methylpyrrolidinone solvent, and 10wt% acetylene black on an Al foil substrate.

3. Results and discussion

Fig. 1(a) shows the XRD patterns of LMO–Sn$_x$ ($0 \leq x \leq 0.05$) and pristine LiMn$_2$O$_4$. All peaks can be indexed by the well-defined spinel phase with the space group of Fd$\bar{3}$m, when $x \leq 0.01$. No impurity peaks corresponding to the Sn compounds were observed. The peak position of XRD patterns shifted to a higher angle with the increase in the Sn amount. This could be because as the Sn ion is substituted into the 16d octahedral site of Mn [25], the large ionic radius of Sn will lead to the peak shifting to a higher angle, as shown in Fig. 1(b). This result indicates that Sn is successfully incorporated into the lattice structure of LiMn$_2$O$_4$. When the Sn content was greater than 0.01, the diffraction peak of SnO$_2$ appeared for the samples, indicating that the Sn ion is soluble in the lattice of LiMn$_2$O$_4$ to a certain extent beyond which it exists in the form of SnO$_2$.

Fig. 2 exhibits the SEM images of pristine LiMn$_2$O$_4$ and LiMn$_2$O$_4$ with different amounts of Sn. After heat treatment, the LMO–Sn$_x$ ($x = 0$, 0.005, and 0.01) products displayed the morphologies of well-crystallized octahedral particles, approximately 400 nm in size, as shown in Fig. 2(a)–(c). An increase in the Sn amount changed the appearance of octahedral particles from clear to vague, and the surface became rough when the Sn content was larger than 0.01 (Fig. 2(d)–(e).

Fig. 3 shows the TEM images of LiMn$_2$O$_4$ samples with different Sn amounts. Fig. 3(a) shows the surface of the pure phase LiMn$_2$O$_4$ is relatively smooth, while the samples with different Sn contents show different surface topography. Fig. 3(b) shows the TEM images of the LiMn$_2$O$_4$ sample with Sn content of $x = 0.005$. Due to the low doping, the particle surface topography seemed discontinuous and uneven. Fig. 3(c)
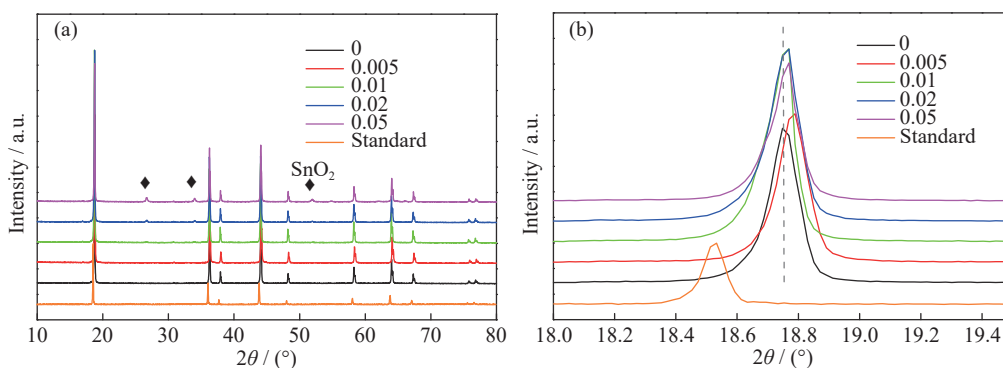

Fig. 1. (a) XRD patterns of LMO–Sn$_x$ ($x = 0$, 0.005, 0.01, 0.02, and 0.05) and the standard XRD pattern of LiMn$_2$O$_4$ and (b) the enlarged image of peaks shifting to a higher angle.
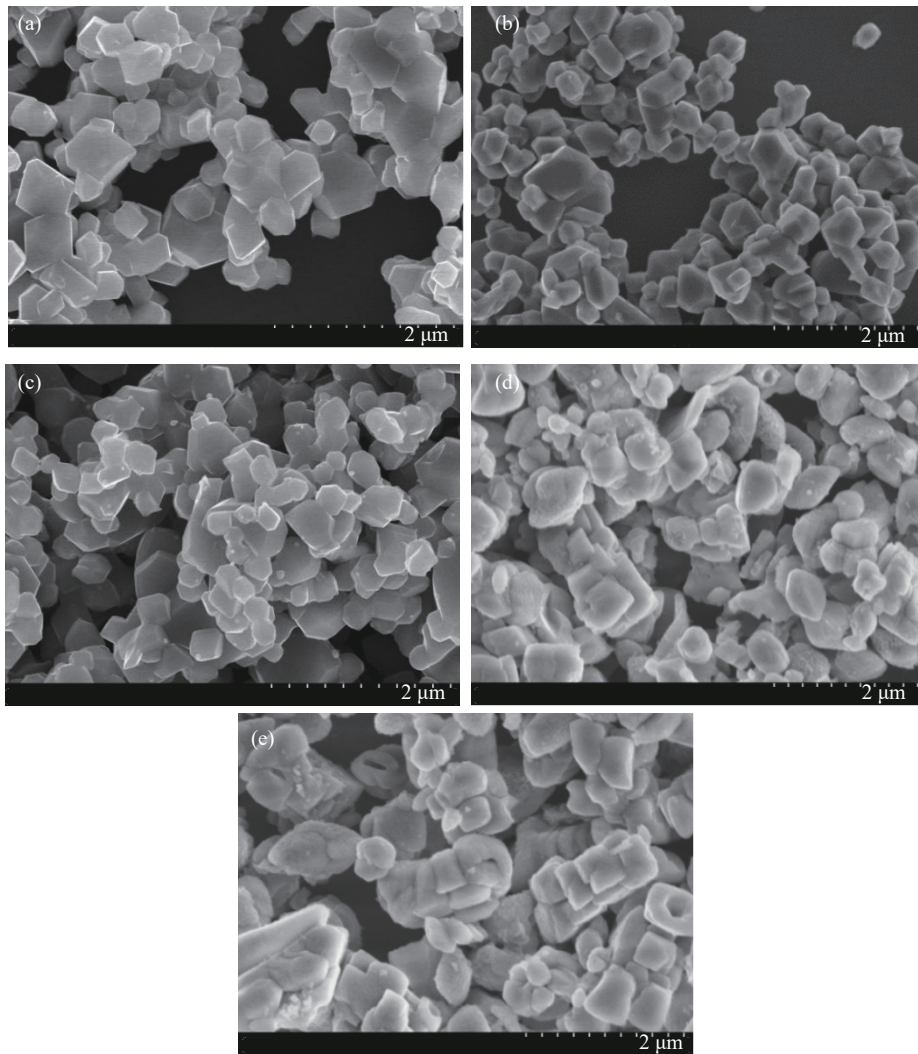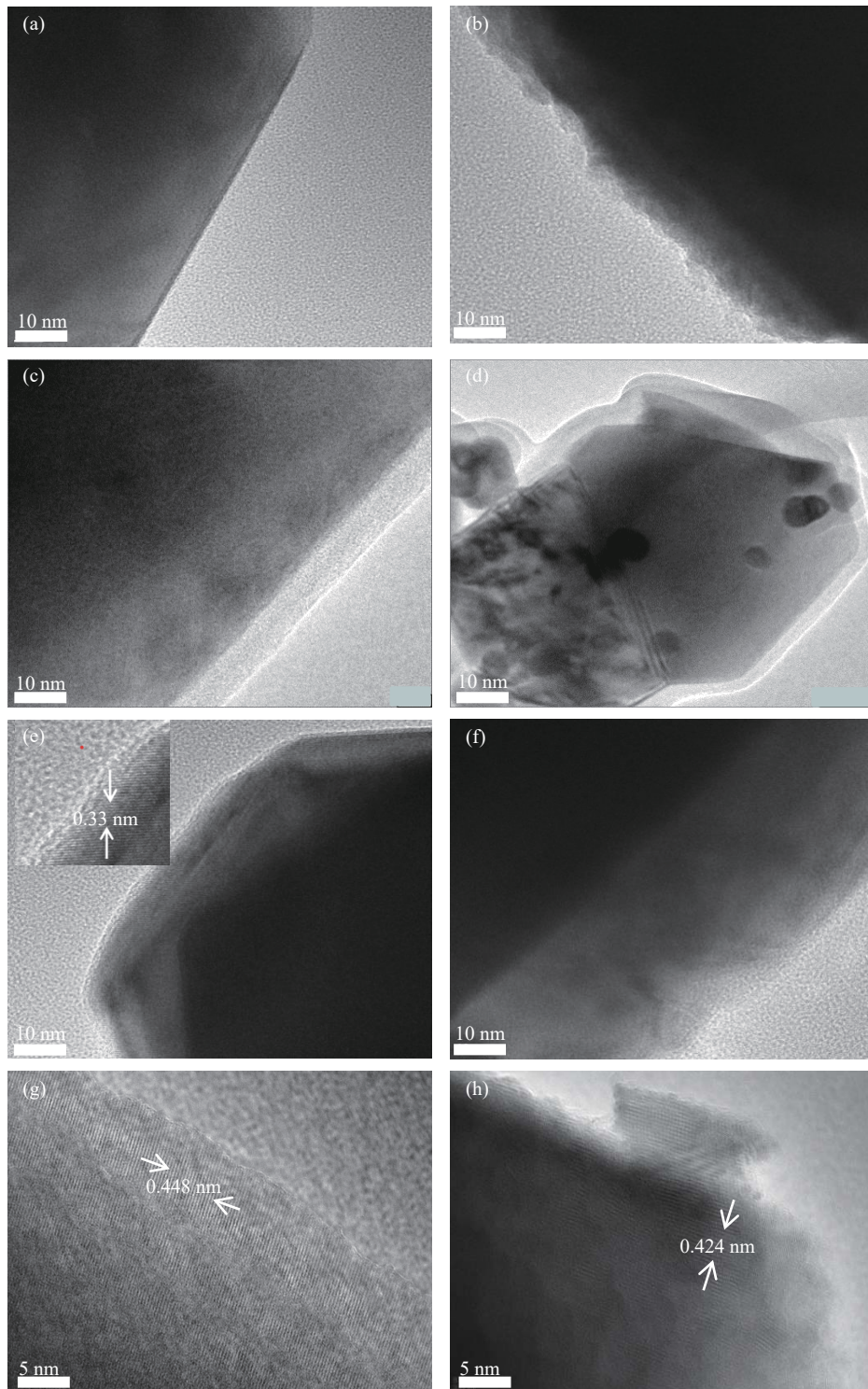
Fig. 2.   SEM images of LMO–Sn$_x$: (a) $x = 0$, (b) $x = 0.005$, (c) $x = 0.01$, (d) $x = 0.02$, and (e) $x = 0.05$.

and (d) shows that when the Sn content increases to $x = 0.01$, a uniform and smooth coating layer with a thickness of about 5 nm appears. This may prevent the corrosion of material surface by the electrolyte, inhibit the dissolution of manganese ions, and improve the cycle stability. When the Sn content is 0.02 or 0.05, the particle surface is covered with a 10–30 nm-thick coating layer, as shown in Fig. 3(e) and (f). This thick coating may decrease the specific capacity of the material owing to its low conductivity. The high-resolution TEM analysis of the sample with $x = 0.02$ shows that the coating layer is SnO_2, characterized with the (110) planes of a lattice spacing of 0.33 nm for SnO_2, which is consistent with the SnO_2 peaks obtained from XRD [26]. Meanwhile, HRTEM images showed that the crystal plane spacing of the pristine $LiMn_2O_4$ is 0.448 nm, corresponding to the (111) planes of the $LiMn_2O_4$ spinel phase structure, as shown in Fig. 3(g). The crystal plane spacing changes to 0.424 nm after Sn doping ($x = 0.005$), indicating that the dopant enters the lattice position and decreases the crystal plane spacing, as shown in Fig. 3(h).

Fig. 4 shows the selected particle analysis locations of LMO–Sn$_x$ when $x = 0.005$ (Fig. 4(a)) and $x = 0.01$ (Fig. 4(c)), and Fig. 4(b) and (d) shows the corresponding analysis res-ults of Sn and Mn using the Auger electron energy spectrum. Sn and Mn show clearly different trends with the increase of detection depth. From the edge of the particles to 10 nm inside, Mn shows an increasing trend, while Sn decreases. The strong Sn signal at the particle edge demonstrates the Sn-rich surface layer of Sn-doped $LiMn_2O_4$.

The XPS spectra of Mn and Sn for LMO–Sn$_x$ were overlaid for comparison. The binding energy of the peak maxima for Mn of LMO–Sn$_x$ shifted toward a higher energy with x from 0.00 to 0.01 (Fig. 5(a)), suggesting a decreased contribution of the Mn(III) species over the substitution range of Sn; however, the peak shifted to a lower energy when $x = 0.02$ and 0.05, indicating the increase in Mn(III) content. To obtain further information on the Mn percentage at the surface of LMO–Sn$_x$, the Mn 2P$_{3/2}$ XPS spectra were fitted using the XPSPEAK 4.1 software. The Mn XPS spectra in Fig. 5(b) represent the manganese content, which can be used to calculate the average valence state of Mn between Mn³⁺ and Mn⁴⁺. When the binding energy positions of Mn³⁺ and Mn⁴⁺ are fixed at 642.1 and 643.6 eV, respectively, deconvolution can be conducted accurately [27]. The valence states in the $x = 0.005$ and 0.01 samples were determined as 3.54 and 3.59, respectively, which are higher than the 3.50 value for pristine

Fig. 3. TEM images for the particle edge of LMO–Sn$_x$: (a) $x = 0$, (b) $x = 0.005$, (c, d) $x = 0.01$, (e) $x = 0.02$, and (f) $x = 0.05$. Inset in (e) shows the lattice spacing of coating layer for LMO–Sn$_x$ with $x = 0.02$. HRTEM images of (g) pristine LiMn$_2$O$_4$ and (h) LMO–Sn$_x$ with $x = 0.005$.

LiMn$_2$O$_4$. For the Sn contents of $x = 0.02$ and 0.05, the valance states were 3.53 and 3.52, respectively. This slight increase in the valence state is related to the substitution of Mn^{3+} at the octahedral site (16d) by Sn^{2+} to maintain charge neutrality. The XPS spectra of Sn 3d$_{3/2}$ and Sn 3d$_{5/2}$ of LMO–Sn$_x$ are shown in Fig. 5(c), resulting from the spin-orbit splitting. The peak points of both Sn 3d$_{3/2}$ and Sn 3d$_{5/2}$ shifted to a lower binding energy for $x = 0.005$ and 0.01, in-

dicating that the relative content of Sn^{2+} is greater than that of Sn^{4+} at a lower Sn content; however, when Sn content is high, it moves toward a higher energy owing to the SnO$_2$ coating layer formation. The Sn content could be identified more definitely from the fitted profiles shown in Fig. 5(d). When the binding energy positions of Sn^{2+} and Sn^{4+} were fixed at 485.75 and 486.75 eV, respectively, deconvolution was performed accurately [28]. The average valence of Mn in-
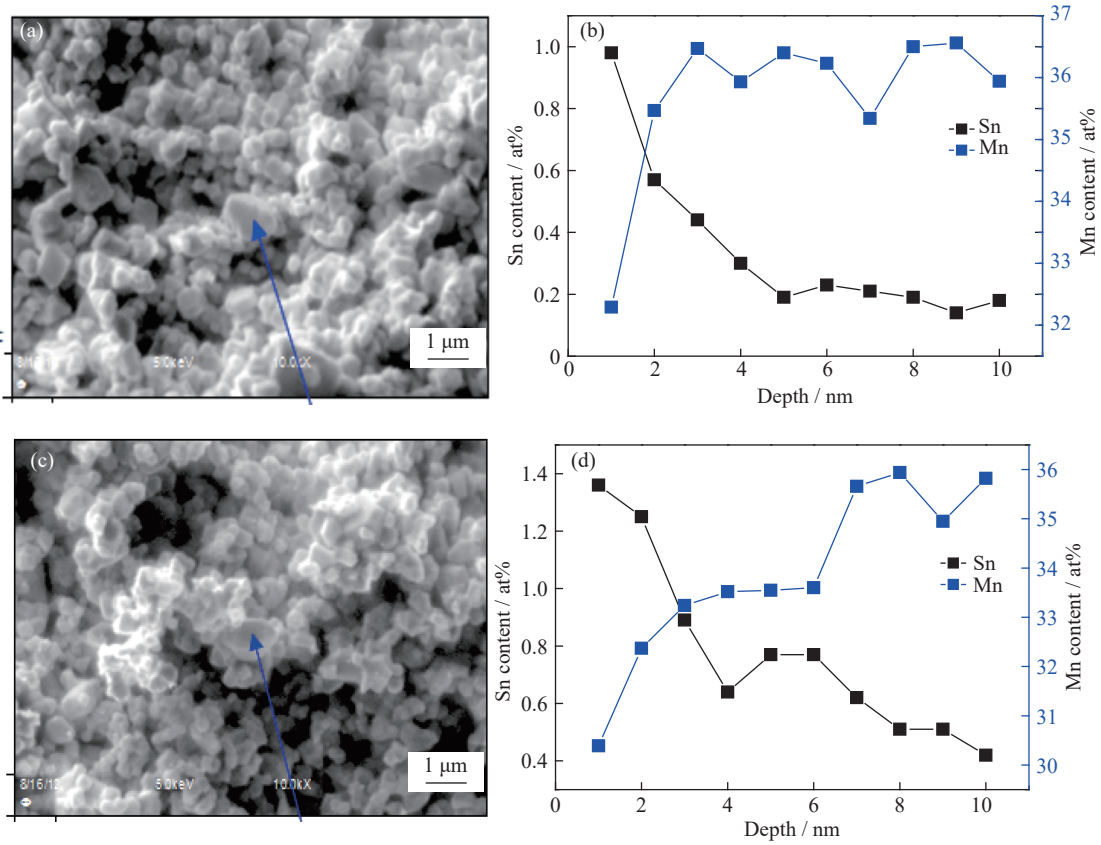
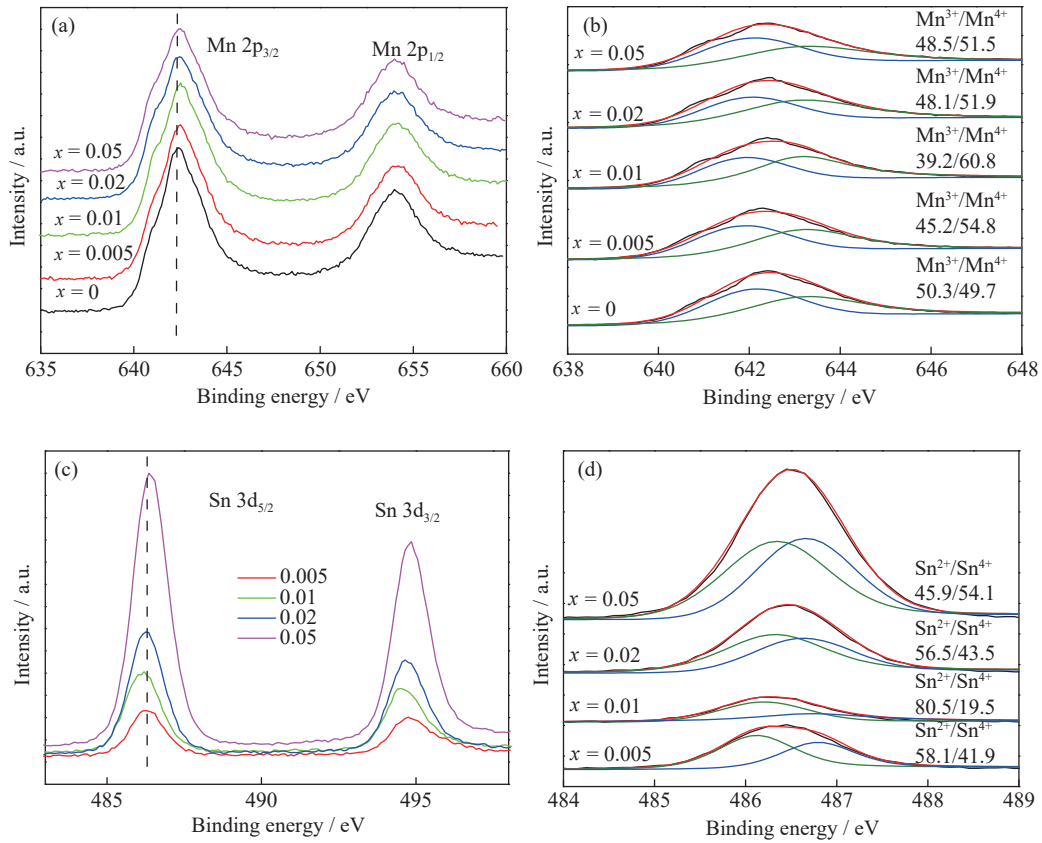Fig. 4.   AES analysis of LMO–Sn$_x$: (a, b) $x = 0.005$ and (c, d) $x = 0.01$.

Fig. 5.   (a) Mn 3p XPS spectra of LMO–Sn$_x$ with different contents of Sn^{2+} as $x = 0$, 0.005, 0.01, 0.02, and 0.05; (b) fitted Mn 2p$_{3/2}$ XPS spectra denoted the respective percentages of the Mn^{3+} contents of 50.3%, 45.2%, 39.2%, 48.1%, and 48.5%; (c) Sn 3d XPS spectra of LMO–Sn$_x$ with different contents of Sn^{2+}; (d) fitted Sn 3d$_{5/2}$ XPS spectra denoted the respective percentages of the Sn^{2+} contents of 58.1%, 80.5%, 56.5%, and 45.9%.

creased for the Sn contents of $x = 0.005$ and 0.01, whereas that of Mn decreased for $x = 0.02$ and 0.05 when the intensity of the SnO$_2$ (110) peak increased. This implies that a small amount of Sn^{2+} replaces Mn^{3+} with limited solubility, and the remaining Sn^{2+} is located outside the LiMn$_2$O$_4$ particles as the ion radius of Sn^{2+} (0.0930 nm) is larger than that of Mn^{3+} (0.0785 nm) [29], i.e., the average valence state of Mn decreases when $x > 0.01$.

To further determine the surface phase composite of LiMn$_2$O$_4$ doped with Sn, the K-edge absorption spectrum of O with TEY mode was measured. Fig. 6(a) shows the K-edge absorption spectrum of O in the sample with the Sn content of 0.01 (labeled as exp) and the calculated spectrum of the potential species, including pure LiMn$_2$O$_4$ (LMO), Li$_2$SnO$_3$ (LSO), SnO, and SnO$_2$. The results showed that the three significant feature peaks of LiMn$_2$O$_4$, pre-edge peaks A1 and A2 and peak B, are consistent with the experimental spectrum when the Sn amount is 0.01. When all Mn is replaced by Sn or the surface coating is regarded as an oxide of Sn, the peak

type and peak position of the calculated spectrum line are no longer consistent with the experimental spectrum. Using the fingerprint of the O K-edge XAS, we could easily exclude the possibility of LSO, SnO, and SnO$_2$ presence on the sample surface. As evident, the pre-edge peaks correspond to the transition of O 1s electrons into the hybridized state of the metal 3d with O 2p orbitals. The integral intensity of the pre-edge peak of the O K-edge spectra is related to the total d electron hole number of the hybridized states. Moreover, the A2 peaks are more sensitive to the local environment as compared to the A1 peaks. After Sn doping, there is an enhanced intensity of pre-edge peaks A2, meaning that M–O bond becomes stronger and presents features similar to the experimental spectrum. Combined with the XPS results, it could be inferred that the surface layer contains a small part of Sn^{2+}, changing the valence state of Mn. The calculated spectrum of part Mn replaced by Sn (LMO + S) is consistent with the experiment spectrum. In other words, the surface phase can be determined as LiMn$_{1.99}$Sn$_{0.01}$O$_4$.
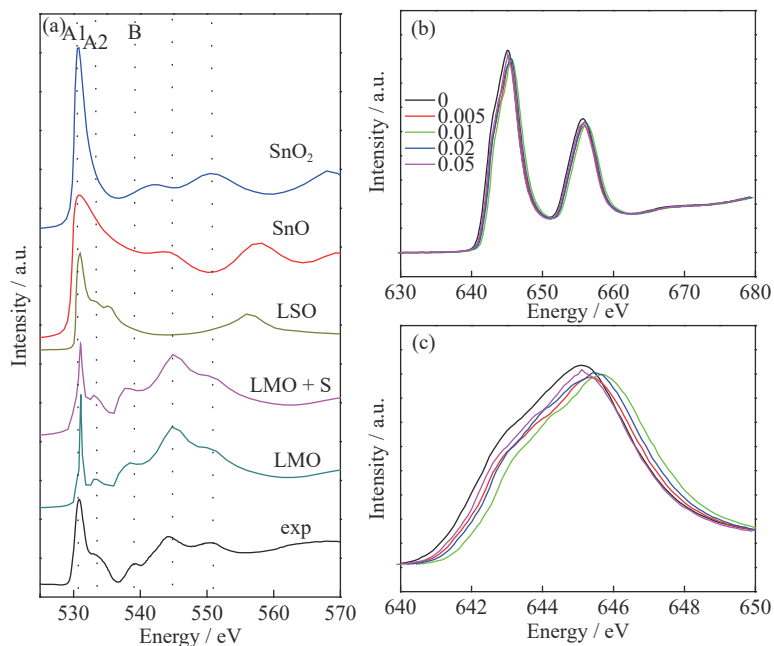

Fig. 6. (a) Peak pattern and peak position of the calculated spectral lines and the experimental spectrum for $x = 0.01$; (b) L edge absorption spectra of Mn and (c) the enlarged image of (b).

Fig. 6(b) shows the L edge absorption spectra of Mn. The edge position shows an evident shift to a higher energy after Sn doping (enlarged image in Fig. 6(c), demonstrating an enhanced Mn valence state. However, when the Sn contents are $x \geq 0.02$, their peak positions shift slightly toward the lower energy. The reason could be that when the Sn^{2+} proportion increases, it is easier to form SnO$_2$ rather than replace Mn^{3+}; thus, the average valence state of Mn decreases.

The cyclic performance of the pristine LiMn$_2$O$_4$ and LiMn$_2$O$_4$ doped with Sn at room temperature with metal lithium as the counter electrode is shown in Fig. 7(a). Since Sn ion is not involved in the redox reaction in LiMn$_2$O$_4$, high tin doping will reduce the capacity of the material. When the Sn content is 0.01, the first discharge capacity is 124 mAh·g^{-1}. After 50 cycles, the discharge capacity drops to 113 mAh·g^{-1}

with a retention rate of 91.1%, which is apparently higher than that of the pristine LiMn$_2$O$_4$ [30]. The increase in the specific capacity after Sn doping can be attributed to the reduced disproportionation reaction of Mn^{3+} and prevents manganese dissolution effectively due to the SnO$_2$ coating layer. Moreover, the enhanced electrochemical performance can be attributed to the increase in conductivity after Sn doping [31]. When the amount of Sn increases to 0.02, the first discharge capacity is 122 mAh·g^{-1}, drops to 110 mAh·g^{-1} after the subsequent 50 cycles. When the amount of Sn is 0.05, the discharge capacity decreases from 113 to 106 mAh·g^{-1} with the same electrochemical process as above. This may be because excessive Sn makes it easy to form SnO$_2$ particles on the sample surface, resulting in increased material impedance and reduced specific capacity. Fig. 7(b) shows the cyclic per-
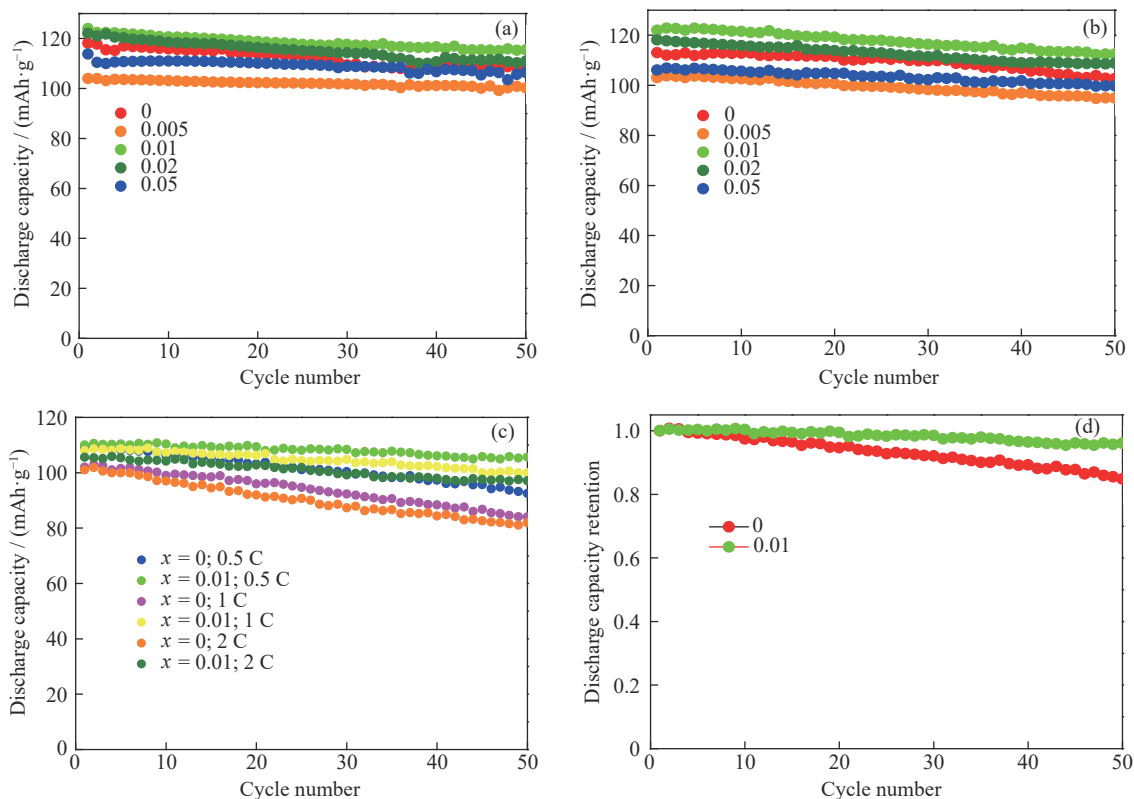
Fig. 7. Cyclic performance of the pristine LiMn$_2$O$_4$ and Sn-doped LiMn$_2$O$_4$ at (a) room temperature and (b) 55°C with metal lithium as the counter electrode; (c) cyclic performance of the pristine LiMn$_2$O$_4$ and Sn-doped LiMn$_2$O$_4$ at 55°C with graphite as the counter electrode; (d) retention rates of the pristine LiMn$_2$O$_4$ and Sn-doped LiMn$_2$O$_4$.

formance of the pristine LiMn$_2$O$_4$ and LiMn$_2$O$_4$ doped with Sn at 55°C. When the doping amount is 0.01, the first discharge capacity at 0.2 C rate was 120 mAh·g^{-1} with a retention rate of 90.2%. When the doping amount is 0.02, the performance is slightly lower but still higher than that of pure lithium manganate.

Fig. 7(c) demonstrates the application of modified material in practice, graphite as an anode, to measure the electrochemical properties at 55°C. For the Sn content of 0.01, the first discharge capacity is 110 mAh·g^{-1} at 0.5 C, with 108 mAh·g^{-1} at 1 C and 105 mAh·g^{-1} at 2 C, while the first discharge capacities of the pristine LiMn$_2$O$_4$ are 109 mAh·g^{-1} at 0.5 C, 102 mAh·g^{-1} at 1 C, and 101 mAh·g^{-1} at 2 C. After 50 cycles, the discharge capacity of the sample with Sn content of 0.01 is 105 mAh·g^{-1} with a retention rate of up to 95.4%, while the discharge capacity of the pristine sample is 92 mAh·g^{-1} with a retention rate of only 84.4%, as shown in Fig. 7(d). The electrochemical performance achieved herein is highly competitive with most reported work on modified LiMn$_2$O$_4$ [32–33]. The high electrochemical performance indicates that the surface-coated LiMn$_2$O$_4$ has better electrochemical cycle stability than the pure phase, especially with the significantly improved high-temperature stability of LiMn$_2$O$_4$. As well-known, the Jahn–Teller effect will aggravate the disproportionation reaction of Mn^{3+}. The resulting Mn^{2+} ion is easily soluble in the electrolyte and destroys the solid electrolyte interface (SEI) film on the anode, declining the battery performance. Moderate Sn doping can enhance the Mn^{4+} content in the material and inhibit Jahn–Teller ef-

fect. Moreover, the Sn-rich coating formed on the surface of LiMn$_2$O$_4$ plays an important role in protecting the material from corrosion by the electrolyte.

4. Conclusion

In conclusion, LiSn$_{0.01}$Mn$_{1.99}$O$_4$ prepared via sol–gel method showed an exceptionally strong cycle ability, with a remarkable capacity retention of 91.1% and 90.2% at the rate of 0.2 C at 25°C and 55°C as well as high initial capacities of 124 mAh·g^{-1} and 120 mAh·g^{-1}, respectively. The properties of the material depended closely on the dopant amount, which is attributed to the fact that an appropriate amount of the Sn dopant can improve the valence state of Mn and inhibit the Jahn–Teller distortion effectively. Our work demonstrates an effective strategy for improving the electrochemical performance of spinel cathode materials with the integration of coating and doping by Sn self-segregation, and it highlights the role of segregation and optimal designing of spinel cathode materials for long-life and low-cost lithium batteries.

Acknowledgements

Conflict of Interest

The authors declare no competing financial interest.

References

[1] J.M. Tarascon and M. Armand, Issues and challenges facing rechargeable lithium batteries, *Nature*, 414(2001), No. 6861, p. 359.

[2] M. Li, J. Lu, Z.W. Chen, and K. Amine, 30 years of lithium-ion batteries, *Adv. Mater.*, 30(2018), No. 33, art. No. 1800561.

[3] L.F. Wang, M.M. Geng, X.N. Ding, C. Fang, Y. Zhang, S.S. Shi, Y. Zheng, K. Yang, C. Zhan, and X.D. Wang, Research progress of the electrochemical impedance technique applied to the high-capacity lithium-ion battery, *Int. J. Miner. Metall. Mater.*, 28(2021), No. 4, p. 538.

[4] Q.K. Du, Q.X. Wu, H.X. Wang, X.J. Meng, Z.K. Ji, S. Zhao, W.W. Zhu, C. Liu, M. Ling, and C.D. Liang, Carbon dot-modified silicon nanoparticles for lithium-ion batteries, *Int. J. Miner. Metall. Mater.*, 28(2021), No. 10, p. 1603.

[5] H.P. Yang, H.H. Wu, M.Y. Ge, L.J. Li, Y.F. Yuan, Q. Yao, J. Chen, L.F. Xia, J.M. Zheng, Z.Y. Chen, J.F. Duan, K. Kisslinger, X.C. Zeng, W.K. Lee, Q.B. Zhang, and J. Lu, Simultaneously dual modification of Ni-rich layered oxide cathode for high-energy lithium-ion batteries, *Adv. Funct. Mater.*, 29(2019), No. 13, art. No. 1808825.

[6] L.J. Li, J.X. Chen, H. Huang, L. Tan, L.B. Song, H.H. Wu, C. Wang, Z.X. Zhao, H.L. Yi, J.F. Duan, and T. Dong, Role of residual Li and oxygen vacancies in Ni-rich cathode materials, *ACS Appl. Mater. Interfaces*, 13(2021), No. 36, p. 42554.

[7] K. Turcheniuk, D. Bondarev, V. Singhal, and G. Yushin, Ten years left to redesign lithium-ion batteries, *Nature*, 559(2018), No. 7715, p. 467.

[8] M. Freire, N.V. Kosova, C. Jordy, D. Chateigner, O.I. Lebedev, A. Maignan, and V. Pralong, A new active Li–Mn–O compound for high energy density Li-ion batteries, *Nat. Mater.*, 15(2016), No. 2, p. 173.

[9] J. Lee, D.A. Kitchaev, D.H. Kwon, C.W. Lee, J.K. Papp, Y.S. Liu, Z.Y. Lun, R.J. Clément, T. Shi, B.D. McCloskey, J.H. Guo, M. Balasubramanian, and G. Ceder, Reversible Mn^{2+}/Mn^{4+} double redox in lithium-excess cathode materials, *Nature*, 556(2018), No. 7700, p. 185.

[10] N. Nitta, F.X. Wu, J.T. Lee, and G. Yushin, Li-ion battery materials: Present and future, *Mater. Today*, 18(2015), No. 5, p. 252.

[11] H. Li, Z.X. Wang, L.Q. Chen, and X.J. Huang, Research on advanced materials for Li-ion batteries, *Adv. Mater.*, 21(2009), No. 45, p. 4593.

[12] F. Li, J. He, J.D. Liu, M.G. Wu, Y.Y. Hou, H.P. Wang, S.H. Qi, Q.H. Liu, J.W. Hu, and J.M. Ma, Gradient solid electrolyte interphase and lithium-ion solvation regulated by bisfluoroacetamide for stable lithium metal batteries, *Angew. Chem. Int. Ed.*, 60(2021), No. 12, p. 6600.

[13] S.H. Qi, H.P. Wang, J. He, J.D. Liu, C.Y. Cui, M.G. Wu, F. Li, Y.Z. Feng, and J.M. Ma, Electrolytes enriched by potassium perfluorinated sulfonates for lithium metal batteries, *Sci. Bull.*, 66(2021), No. 7, p. 685.

[14] D.P. Finegan, A. Vamvakeros, C. Tan, T.M.M. Heenan, S.R. Daemi, N. Seitzman, M.D. Michiel, S. Jacques, A.M. Beale, D.J.L. Brett, P.R. Shearing, and K. Smith, Spatial quantification of dynamic inter and intra particle crystallographic heterogeneities within lithium ion electrodes, *Nat. Commun.*, 11(2020), art. No. 631.

[15] F.Y. Cheng, H.B. Wang, Z.Q. Zhu, Y. Wang, T.R. Zhang, Z.L. Tao, and J. Chen, Porous $LiMn_2O_4$ nanorods with durable high-rate capability for rechargeable Li-ion batteries, *Energy Environ. Sci.*, 4(2011), No. 9, art. No. 3668.

[16] G. Zhou, X.R. Sun, Q.H. Li, X.L. Wang, J.N. Zhang, W.L. Yang, X.Q. Yu, R.J. Xiao, and H. Li, Mn ion dissolution mechanism for lithium-ion battery with $LiMn_2O_4$ cathode: *In situ* ultraviolet–visible spectroscopy and Ab initio molecular dynamics simulations, *J. Phys. Chem. Lett.*, 11(2020), No. 8, p. 3051.

[17] Y.K. Sun, C.S. Yoon, C.K. Kim, S.G. Youn, Y.S. Lee, M. Yoshio, and I.H. Oh, Degradation mechanism of spinel $LiAl_{0.2}Mn_{1.8}O_4$ cathode materials on high temperature cycling, *J. Mater. Chem.*, 11(2001), No. 10, p. 2519.

[18] K.R. Ragavendran, P. Mandal, and S. Yarlagadda, Correlation between battery material performance and cooperative electron-phonon interaction in $LiCo_yMn_{2-y}O_4$, *Appl. Phys. Lett.*, 110(2017), No. 14, art. No. 143901.

[19] S. Lee, Y. Cho, H.K. Song, K.T. Lee, and J. Cho, Carbon-coated single-crystal $LiMn_2O_4$ nanoparticle clusters as cathode material for high-energy and high-power lithium-ion batteries, *Angew. Chem. Int. Ed.*, 51(2012), No. 35, p. 8748.

[20] D.K. Kim, P. Muralidharan, H.W. Lee, R. Ruffo, Y. Yang, C.K. Chan, H.L. Peng, R.A. Huggins, and Y. Cui, Spinel $LiMn_2O_4$ nanorods as lithium ion battery cathodes, *Nano Lett.*, 8(2008), No. 11, p. 3948.

[21] P.A. Lee and J.B. Pendry, Theory of the extended X-ray absorption fine structure, *Phys. Rev. B*, 11(1975), No. 8, p. 2795.

[22] C.R. Natoli, M. Benfatto, C. Brouder, M.F.R. López, and D.L. Foulis, Multichannel multiple-scattering theory with general potentials, *Phys. Rev. B*, 42(1990), No. 4, p. 1944.

[23] A.L. Ankudinov, B. Ravel, J.J. Rehr, and S.D. Conradson, Real-space multiple-scattering calculation and interpretation of X-ray-absorption near-edge structure, *Phys. Rev. B*, 58(1998), No. 12, p. 7565.

[24] T.A. Tyson, K.O. Hodgson, C.R. Natoli, and M. Benfatto, General multiple-scattering scheme for the computation and interpretation of X-ray-absorption fine structure in atomic clusters with applications to SF_6, $GeCl_4$, and Br_2 molecules, *Phys. Rev. B*, 46(1992), No. 10, p. 5997.

[25] D.W. Shin, J.W. Choi, W.K. Choi, Y.S. Cho, and S.J. Yoon, Improved cycleability of $LiMn_2O_4$-based thin films by Sn substitution, *Appl. Phys. Lett.*, 93(2008), No. 6, art. No. 064101.

[26] F.L. Du, Z.Y. Guo, and G.C. Li, Hydrothermal synthesis of SnO_2 hollow microspheres, *Mater. Lett.*, 59(2005), No. 19-20, p. 2563.

[27] T.T. Fang and H.Y. Chung, Reassessment of the electronic-conduction behavior above the Verwey-like transition of Ni^{2+}- and Al^{3+}-doped $LiMn_2O_4$, *J. Am. Ceram. Soc.*, 91(2008), No. 1, p. 342.

[28] W.K. Choi, H.J. Jung, and S.K. Koh, Chemical shifts and optical properties of tin oxide films grown by a reactive ion assisted deposition, *J. Vac. Sci. Technol. A*, 14(1996), No. 2, p. 359.

[29] R.D. Shannon, Revised effective ionic radii and systematic studies of interatomic distance in halides and chalcogenides, *Acta Crystallogr. Sect. A*, 32(1976), No. 5, p. 751.

[30] H.R. Taghiyari, K. Mobini, Y.S. Samadi, Z. Doosti, F. Karimi, M. Asghari, A. Jahangiri, and P. Nouri, Effects of nano-wollastonite on thermal conductivity coefficient of medium-density fiberboard, *J. Nanomater. Mol. Nanotechnol.*, 2(2013), No. 1, art. No. 1000106.

[31] Y.L. Ding, J. Xie, G.S. Cao, T.J. Zhu, H.M. Yu, and X.B. Zhao, Single-crystalline $LiMn_2O_4$ nanotubes synthesized via template-engaged reaction as cathodes for high-power lithium ion batteries, *Adv. Funct. Mater.*, 21(2011), No. 2, p. 348.

[32] P.W. Li, S.H. Luo, J.C. Wang, X. Wang, Y. Tian, H. Li, Q. Wang, Y.H. Zhang, and X. Liu, Preparation and electrochemical properties of Al–F co-doped spinel $LiMn_2O_4$ single-crystal material for lithium-ion battery, *Int. J. Energy Res.*, 45(2021), No. 15, p. 21158.

[33] C. Zhan, X.P. Qiu, J. Lu, and K. Amine, Tuning the Mn deposition on the anode to improve the cycle performance of the Mn-based lithium ion battery, *Adv. Mater. Interfaces*, 3(2016), No. 11, art. No. 1500856.